Medium-energy ion scattering structural study of the Ni(111)$(\sqrt{3}\times\sqrt{3})R30°$-Pb surface phase

D. Brown, P. D. Quinn, and D. P. Woodruff

Physics Department, University of Warwick, Coventry CV4 7AL, United Kingdom

P. Bailey and T. C. Q. Noakes

CLRC Daresbury Laboratory, Daresbury, Warrington WA4 4AD, United Kingdom

(Received 5 October 1999)

The structure of the Ni(111)$(\sqrt{3}\times\sqrt{3})R30°$-Pb surface phase formed by a nominal $\frac{1}{3}$ monolayer of Pb has been investigated by medium-energy ion scattering using 100 keV H$^+$ ions in three different incidence directions. The results show clearly that the Pb atoms occupy fcc hollow sites at the surface, but also favor a structure in which these are surrounded by Ni atoms to form a surface alloy phase. A surface alloy with a surface stacking fault, as has been found for the $(\sqrt{3}\times\sqrt{3})$ surface alloy phases formed by Sb adsorption on Cu(111) and Ag(111), can be clearly excluded. The preference for a surface alloy structure is consistent with the results of an earlier low-energy ion scattering study, but we find significant differences in the quantitative structural parameters. This structural model also implies a considerable reduction of the effective radius of the Pb atoms relative to their size in bulk Pb, and this is discussed in the context of other quantitative structural studies of substitutional surface alloy phases

I. INTRODUCTION

During the last few years there has been a growing recognition that metal and semimetal surface adsorption phases on metal surfaces frequently involve the creation of surface alloys, even in cases in which the constituent elements are immiscible in the bulk. In the simplest such cases the adsorbate species substitutes some fraction of the outermost layer atoms of the substrate to form an ordered phase. Specific examples include 0.5 monolayer (ML) $c(2\times2)$ phases on fcc (100) surfaces, such as Au (Refs. 1–3) and Mn on Cu(100),[4,5,3] and 0.33 ML $(\sqrt{3}\times\sqrt{3})R30°$ phases on fcc (111) surfaces, such as Sb on Cu(111) (Refs. 6, 7) and Ag(111) (Refs. 8,6,9) and Na,[10–12] K,[13] and Rb (Refs. 14, 15) on Al(111). As yet the full extent of this phenomenon has not been established, and one related question is the magnitude of the surface corrugation that can result from this surface layer alloying of atoms of different metallic radius. For example, the alkali metals have unusually large metallic radii relative to most other metals, and yield corrugations of the surface alloy ''layer'' on the Al(111) surface which can be as large as the bulk layer spacing. An interesting case in this respect is also the Cu(100)$c(2\times2)$-Mn phase in which the corrugation amplitude is found to be anomalously large, attributed to an enhanced effective radius of the Mn atoms due to the high local spin state which these atoms adopt in this phase.[16]

Recent studies of the Cu(111)$(\sqrt{3}\times\sqrt{3})R30°$-Sb and Ag(111)$(\sqrt{3}\times\sqrt{3})R30°$-Sb surfaces have revealed yet another surprising feature. Interest in these surfaces stems in part from the role of Sb as a surfactant in homoepitaxial growth of Ag on Ag(111),[17,18] and there were early theoretical predictions that the Sb does adopt substitutional sites on this surface.[19] While early coaxial impact collision ion scattering spectroscopy (CAICISS) provided experimental support for this conclusion,[8] recent surface x-ray diffraction (SXRD) studies of both surfaces,[6] a medium-energy ion scat-

tering (MEIS) study of the Cu(111)$(\sqrt{3}\times\sqrt{3})R30°$-Sb surface,[7] and a quantitative low-energy electron diffraction (LEED) study of Ag(111)$(\sqrt{3}\times\sqrt{3})R30°$-Sb (Ref. 9) all conclude that while Sb does substitute outermost layer substrate atoms, the whole surface alloy layer is laterally displaced to produce a stacking fault at the substrate/alloy interface.[20] In this alloy layer all atoms then occupy so-called hcp hollow sites (directly above atoms in the second layer of the underlying nonreconstructed substrate) rather than the proper fcc hollow sites (above atoms in the third layer of the underlying substrate). The driving force for this surprising surface structure remains unclear. However, in view of this result it is clearly of interest to establish the true structure of other (111)$(\sqrt{3}\times\sqrt{3})R30°$ metal overlayer phases.

Here we present the results of a MEIS study of the structure of the Ni(111)$(\sqrt{3}\times\sqrt{3})R30°$-Pb surface. A recent CAICISS investigation of this surface[21] concluded that this phase does involve substitution of the Pb atoms into the outermost layer to form a surface alloy, but did not consider the possibility of a stacking fault in the analysis. In this regard we note that the MEIS and CAICISS techniques are somewhat complementary in such investigations; MEIS has significantly greater subsurface penetration and is therefore potentially more sensitive to subsurface registry changes, but CAICISS is intrinsically more surface specific and so should be better suited to distinguishing substitutional and overlayer surface phases. Our results show clearly that this surface phase does not involve any stacking fault, but do also favor the alloy interpretation. A key quantitative structural parameter is the amplitude of the corrugation in the surface alloy, which we find to be significantly larger than that obtained from the CAICISS investigation. However, even our larger value indicates a strong modification of the effective radius of the Pb adsorbate atoms relative to its value in bulk Pb. The significance of this result is discussed in the context of previous related measurements of other surface alloy phases.

II. EXPERIMENTAL DETAILS

All experimental work reported in this study was performed at the U.K. MEIS facility based at the CLRC Daresbury Laboratory. A Ni(111) substrate, approximately 12 mm diameter$\times$2 mm thickness, was initially prepared by x-ray Laue alignment, spark machining, and mechanical polishing prior to mounting into the ultrahigh-vacuum MEIS preparation chamber where it was cleaned by repeated cycles of sputtering with 1 keV Ar^+ ions and subsequent annealing to 923 K. Surface composition and ordering were verified *in situ* by Auger electron spectroscopy (AES) and LEED, respectively. Pb was deposited from a Knudsen cell operated at 873 K on to the Ni(111) substrate maintained at an approximate temperature of 323 K. During Pb deposition, the peak-to-peak amplitudes of the Ni $M_{2,3}M_{4,5}M_{4,5}$ (61 eV) and Pb $N_{6,7}O_{4,5}O_{4,5}$ (94 eV) Auger electron signals were obtained from the derivative Auger spectrum. A plot of the ratio of the intensities as a function of Pb deposition time revealed a change in slope after 19 min. According to Umezawa *et al.*,[22] this corresponds to completion of the first complete layer at a coverage of 0.54 ML defined with respect to the ideal Ni(111) surface area density of 1.86 $\times 10^{15}$ atoms cm^{-2}. Consequently, the deposition rate was calibrated at approximately 0.03 ML min^{-1}. LEED patterns at various Pb-coverages (θ_{Pb}) were also recorded. A (1 $\times$1) pattern was retained for $\theta_{Pb}<0.3$ ML. For $0.3<\theta_{Pb} <0.5$ ML a (3$\times$3) pattern emerged, followed by a (4$\times$4) pattern at $\theta_{Pb}>0.5$ ML. This result is broadly consistent with the earlier study of this overlayer growth system.[22]

The Ni(111)($\sqrt{3}\times\sqrt{3}$)$R30°$-Pb surface phase was prepared utilizing a method outlined by Umezawa and co-workers.[21] This involved deposition of Pb on to the Ni(111) crystal to a nominal coverage of 0.45 ML. At the completion of this stage, the initial (1$\times$1) LEED pattern of the clean surface was transformed into a (3$\times$3) pattern. The crystal was then annealed at 873 K for several seconds. After allowing the sample to cool to ambient temperature, a strong ($\sqrt{3}\times\sqrt{3}$)$R30°$ pattern emerged. However, on closer inspection, a very faint background of residual (3$\times$3) spots was observed. Attempts to completely remove the Ni(111)(3$\times$3)-Pb impurity phase by varying the annealing conditions only led to a degradation in the quality of the ($\sqrt{3}\times\sqrt{3}$)$R30°$ LEED pattern. The results presented here therefore correspond to the original preparation treatment in which a small fraction of the surface (almost certainly no more than 10%) is covered with the (3$\times$3) phase.

The MEIS facility together with methods of data acquisition and reduction has been described in earlier publications[7,3] and a more general review of the MEIS technique can be found elsewhere.[23] The basic approach is to use incident ion directions that illuminate only a small number of near-surface layers and to then determine the relative positions of the atoms in these layers by studying the angular locations of the ''blocking'' dips in the scattered signal which results from nearest-surface atoms obscuring the scattered signal from subsurface atoms. The scattering ion signal was detected using an electrostatic dispersive analyzer equipped with a two-dimensional detector to allow simultaneous collection of data at a range of scattering angles and scattered ion energies. Ion scattering measurements were
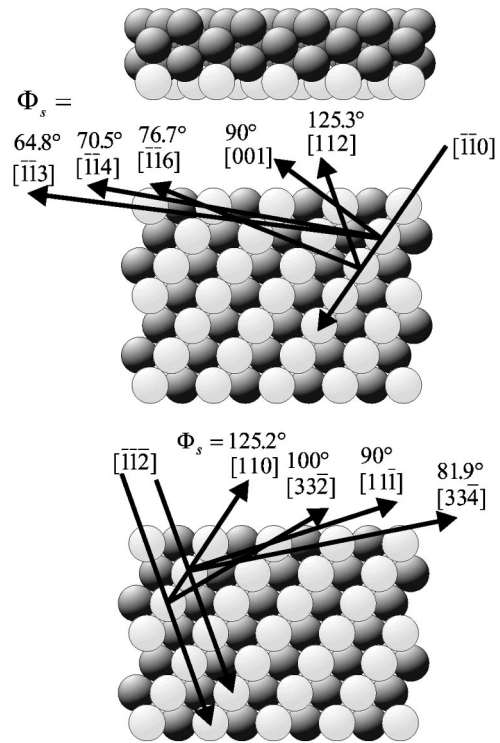

FIG. 1. Schematic diagrams showing the scattering geometries used in this study in the $\langle 112 \rangle$ azimuth relative to an ideally terminated Ni(111) clean surface. At the top of the figure a top view of a slab of the surface is shown extended in the scattering plane but only a few atomic spacings wide perpendicular to this plane. In this azimuth, all atoms in the crystal are contained within a single set of identical atomic planes containing atoms in all layers. A single such plane is shown with the atoms shown as light balls to distinguish them from the other dark atoms, and two equivalent side views of this plane are shown to illustrate the two different incidence and scattering geometries. Note that the principal blocking directions correspond approximately to the main dips in the experimental data for the Pb-covered surface (Figs. 3 and 4 below) although slight modifications in angles result from adsorbate-induced structural modifications.

performed with the sample at ambient temperature, employing 100 keV H^+ ions incident along $[\bar{1}\,\bar{1}0]$, $[\bar{1}\,\bar{1}\,\bar{2}]$, and $[\bar{1}\,\bar{2}\,\bar{3}]$ crystallographic directions. These incidence geometries and some of the associated blocking directions for the clean surface are illustrated in Figs. 1 and 2 and discussed in more detail later in the paper. Due to the large difference in scatterer masses, the Pb and Ni scattering signals were fully resolved across the entire range of scattering angles employed. Blocking curves were obtained by integration of the Ni signal over a range of (inelastic) scattered ion energies corresponding, approximately, to the depth of the first six atomic layers. Complete data sets were obtained by summing blocking curves from at least two freshly prepared surfaces. In order to obtain an absolute calibration of the scattered ion yield, the incident ion dose received by the sample was determined by measuring the total charge arriving at a tungsten mesh (70% transmission) positioned in the beam path and surrounded by a biased shield to eliminate secondary electron contributions. The dimensions of the beam spot for normal incidence are 1.0 mm (horizontal)$\times$0.5 mm (vertical). The total incident ion fluxes corresponding to the scattered
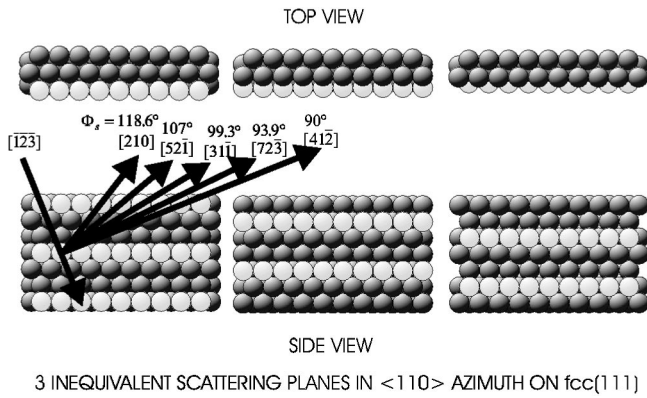
FIG. 2. Schematic diagrams showing the scattering geometries used in this study in the $\langle 110 \rangle$ azimuth relative to an ideally terminated Ni(111) clean surface. In this azimuth there are three inequivalent planes of atoms which make up the crystal, one containing atoms in layers 1,4,7, etc., a second containing atoms in layers 2,5,8, etc., and the third containing atoms in layers 3,6,9, etc. These three different planes are shown with the associated atoms shown as light balls (successive layers being removed from the cluster as seen in the top view). The incident and blocking directions are shown on just the first of these planes, but each plane contains the same blocking events simply transposed perpendicular to the surface by the appropriate number of layer spacings. Note that the principal blocking directions correspond approximately to the main dips in the experimental data for the Pb-covered surface (Figs. 3 and 4 below) although slight modifications in angles result from adsorbate-induced structural modifications.

signals measured were 1.4×10^{16}, 1.7×10^{16}, and 1.1×10^{16} ions cm^{-2} in the $[\bar{1}\,\bar{1}0]$, $[\bar{1}\,\bar{1}\,\bar{2}]$, and $[\bar{1}\,\bar{2}\,\bar{3}]$ incidence geometries, respectively. In order to minimize sample damage, the position of the incident beam spot on the surface was changed regularly throughout the period of data acquisition. The resulting ion fluxes on any part of the sample were typically within the range utilized in similar MEIS studies.[24]

III. EXPERIMENTAL RESULTS AND STRUCTURE ANALYSIS

Ion scattering data were obtained for the Ni(111)$(\sqrt{3} \times \sqrt{3})R30°$-Pb surface phase in $[\bar{1}\,\bar{1}0]$, $[\bar{1}\,\bar{1}\,\bar{2}]$, and $[\bar{1}\,\bar{2}\,\bar{3}]$ incidence geometries as described in the previous section. Structural analysis involved comparison of the experimental data with simulated blocking curves based on competing structural models. Four possibilities were considered: (i) a "fcc overlayer" with Pb atoms adsorbed in fcc hollow sites; (ii) a "hcp overlayer" with Pb atoms adsorbed in hcp hollow sites; (iii) a "fcc alloy" with Pb atoms incorporated into the outermost Ni layer to form a substitutional surface alloy; and (iv) a "hcp alloy" with Pb and Ni atoms again forming a substitutional alloy, but with all top-layer atoms (both Ni and Pb) displaced laterally onto hcp sites, leading to a substrate/alloy-layer stacking fault. Less plausible overlayer structures, such as those involving Pb adsorption at atop or bridge sites, were not considered.

Simulations involved Monte Carlo modeling utilizing the VEGAS computer code.[25] A Thomas-Fermi-Molière scattering potential was assumed for the theoretical calculations and the

incident and backscattered ion tracks were not connected. In order to achieve a suitable compromise between statistical noise levels and computational time required, shadowing and blocking fluxes of 1×10^{20} and 5×10^{19} ions cm^{-2}, respectively, were employed. The number of layers used to model the near-surface region probed by the MEIS experiment differed slightly for the different scattering geometries and structural models. In the case of the $[\bar{1}\,\bar{1}0]$, and $[\bar{1}\,\bar{1}\,\bar{2}]$ incident geometries, simulations of scattering from the overlayer models used a five-layer slab of Ni atoms, together with the adsorbed Pb atoms; for scattering in these geometries from the substitutional surface alloy models, the five-layer slab included the outermost Ni$_2$Pb alloy layer. For the $[\bar{1}\,\bar{2}\,\bar{3}]$ incidence geometry, which illuminates deeper layers (see below), one extra Ni subsurface layer was included except in the case of the hcp alloy model (iv), for which two extra Ni subsurface layers were added. In all of these cases the number of layers was chosen to ensure convergence in the appropriate incidence direction. The principal parameters varied for each model structure to establish optimum fits were the Pb-Ni and Ni-Ni outermost layer spacings, z_{Pb} and z_{12} respectively. In the case of the overlayer models, these correspond to the layer spacing of the adsorbed Pb atoms above the outermost Ni layer and the first-to-second Ni layer spacings. For the surface alloy models, the comparable parameters were the layer spacings of the Pb and Ni atoms in the surface alloy phase relative to the underlying, outermost pure Ni layer. Notice that the nomenclature labels the outermost Ni layer as "1" in all structures, but in the overlayer models this is a complete unreconstructed layer, whereas in the case of the alloy models it comprises the 0.67 ML of Ni in the alloy phase. For the overlayer models the Pb-Ni layer spacings were varied around the value to be expected from a simple hard-sphere model using metallic radii (half the nearest-neighbor separation in the elemental metal) 1.25 Å for Ni and 1.75 Å for Pb. These imply a Pb-Ni layer spacing value of 2.63 Å for hollow-site occupation on Ni(111). Ni-Ni layer spacings were varied around the nominal bulk value of 2.035 Å. The Ni-Ni and Pb-Ni layer spacings were varied independently in the calculations, so in the case of the surface alloy models both negative and positive corrugations of this surface phase were tested; we define the corrugation amplitude as positive when the Pb atoms are displaced outward relative to the plane of the alloy-layer Ni atoms. For all the theoretical models, uncorrelated, root-mean-square vibrational amplitudes were derived from the corresponding bulk and surface Debye temperatures calculated by Jackson.[26] Tests with other values did not lead to any improvements of the fits.

The quality of fit between the scattering-angle dependence of the experimental (I_{exp}) and theoretical (I_{theory}) scattering yields was evaluated by means of a reliability factor (R_χ) based on a χ-squared criterion,[27] such that

$$R_\chi = 1/N \sum_{i=1}^{i=N} [(I_{exp} - \lambda I_{theory})^2 / I_{exp}]. \quad (1)$$

where N is the number of scattering angles (Φ_s) employed in the data set. In order to compare the experimental yield, defined in terms of ion counts, with the theoretical yield, defined in terms of Ni monolayers illuminated, a scaling factor

λ is employed; this parameter can be determined from calibration experiments as discussed below. Notice that the absolute value of R_χ has no general significance, since it depends on the total number of detected ions in a given data set. Simulated curves were smoothed by means of a moving average and normalized by $1/\sin^4(\Phi_s/2)$ to account for the angular dependence of the scattering cross section.[23] Comparison of theoretical and experimental blocking curves showed a small (5–10 %) residual relative ''tilt'' which was removed by multiplication by a second-order polynomial; this helps to emphasize the quality of the fit to the angular locations and shapes of the blocking features. The lower R factor values that result enhanced the sensitivity to structural parameters.

The choice of this R factor has important advantages in statistical significance because it is based on the actual number of measured ions, which should be governed by Poisson statistics.[7,27] However, because the elastic scattering cross section is strongly dependent on scattering angles and the data were collected using a constant incident ion flux, the blocking curves show a much higher number of scattered ions at the smallest scattering angles. For example, for the $[\bar{1}\,\bar{1}\,\bar{2}]$ and $[\bar{1}\,\bar{2}\,\bar{3}]$ incidence geometries, the counts detected at the highest scattering angle were only about 20% of those detected at the lowest scattering angles. This effect is even larger for the $[\bar{1}\,\bar{1}0]$ data set, due to the slightly larger angular range. This leads to a bias in the R factor to structural models that optimize the fit to the small-scattering-angle data. Note that this part of the data range corresponds to the most grazing emission directions which in turn provides blocking dips whose angles are most sensitive to movements in the surface atoms.

In using MEIS to determine surface geometries, we have explored two different approaches to the scaling factor λ, which relates the absolute signal levels in the experiment and theory. One is to allow λ to vary freely as part of the fitting procedure; the other is to obtain a value of this parameter from a suitable calibration experiment. The use of a freely varying λ allows comparison of the shapes of the blocking curves for different structural models with experiment, and has been found to be quite successful in optimizing structural parameters in MEIS,[7] but important information concerning the absolute yield is lost. This yield can be expressed as an effective number of layers ''seen'' by the incident ion beam; for a rigid, bulk-terminated (111) crystal these values are one layer for $[\bar{1}\,\bar{1}0]$ incidence, two layers for $[\bar{1}\,\bar{1}\,\bar{2}]$ incidence (see Fig. 1), and three layers for $[\bar{1}\,\bar{2}\,\bar{3}]$ incidence (see Fig. 2), all lower-lying atoms being shadowed by these atoms in the outermost layers. Notice that the greater intrinsic penetration on the $[\bar{1}\,\bar{2}\,\bar{3}]$ incidence direction is the reason why we need to use more layers in our model simulations to ensure reasonable convergence. Of course, the actual number of layers seen in each incidence direction will be larger than these numbers due in part to thermal vibrations, but more interestingly due to static atomic displacements (reconstruction) of the surface, which move surface atoms out of bulk-shadowing directions and lead to additional signal from sub-surface layers. The absolute yields thus provide important structural information in addition to the shape of the blocking curves. Of course, absolute calibration of these yields is

potentially susceptible to systematic errors, so our strategy for using such values must take account of possible errors, and specifically allows some adjustment of the exact scaling factor within the structural optimization.

Two methods of absolute calibration to determine λ have been investigated. The first was based on a standard MEIS reference sample, the $Si(111)(\sqrt{3}\times\sqrt{3})R30°$-Au surface, prepared as previously described in the literature,[28] and reported to correspond to a Au coverage of 0.84 ± 0.04 ML. MEIS experiments were conducted using 100 keV H^+ ions incident along the $[\bar{1}\,\bar{1}1]$ crystallographic direction, averaging over different points on the sample surface to ensure uniformity of Au coverage. The Au and Si surface peaks were completely resolved, allowing integration of the Au signal at each scattering angle employed. The number of counts corresponding to the yield expected from a monolayer of Ni atoms in an ideal (111) plane at normal incidence per unit dose on target, $I_{Ni}(\Phi_n)$ was then calculated from the integrated Au signal $I_{Au}(\Phi_s)$ at each scattering angle Φ_s using the expression

$$I_{Ni}(\Phi_n) = \frac{I_{Au}(\Phi_s)\sin^4(\Phi_s/2)\cos(\Phi_i)\sigma_{Ni}\Omega_{Ni}}{\Theta_{Au}N_{H^+}\cos(\Phi_n)\sigma_{Au}\Omega_{Si}}. \qquad (2)$$

The $\sin^4(\Phi_s/2)$ term accounts for the angular dependence of the Rutherford scattering cross section. Θ_{Au} is the Au coverage in ML and N_{H^+} the measured total ion dose received at the target. The cosine terms correct for differences in the incident beam ''footprint'' between normal incidence ($[\bar{1}\,\bar{1}\,\bar{1}]$, $\Phi_n = 0°$) and $[\bar{1}\,\bar{1}1]$ incidence ($\Phi_i = 70.5°$). σ_{Ni} and σ_{Au} are the scattering cross sections for Ni and Au, while Ω_{Si} and Ω_{Ni} are the area densities of ideal (111) planes of Si and Ni, respectively. The final value obtained for $I_{Ni}(\Phi_n)$ was taken as the average over all scattering angles.

The second method to obtain an absolute calibration value was based on MEIS measurements from a clean, unreconstructed Ni(111) surface (also using 100 keV H^+ ions and $[\bar{1}\,\bar{1}1]$ incidence). The resulting blocking curve was fitted by VEGAS simulations, optimizing the value of the outermost Ni-Ni layer spacing which was found to be within 1% of the bulk value, consistent with a previous structural analysis.[29] The optimum values of the isotropic, uncorrelated root-mean-square surface vibrational amplitudes were 0.13 ± 0.02 Å. The experimental yield in counts was then normalized to the best-fit theoretical yield and corrected to account for the ion dose and beam footprint, using independent measurements from two freshly prepared surfaces. Averaging these measurements, together with the Au/Si(111) data, gave a final calibration value of 21.7 ± 0.5 counts $ML^{-1}\mu C^{-1}$ ion dose on the target for Ni(111) at normal incidence.

Using this calibration, the MEIS data from the $Ni(111)(\sqrt{3}\times\sqrt{3})R30°$-Pb surface could also be used in a similar way to determine the Pb coverage; the average value from the three incidence directions was 0.28 ± 0.03 ML, in excellent agreement with the value of 0.29 ± 0.03 ML previously determined for this surface phase by Rutherford backscattering.[21] The fact that this coverage is slightly less than the 0.33 ML expected for an ideal $(\sqrt{3}\times\sqrt{3})R30°$ structure could be due to island formation, although Umezawa
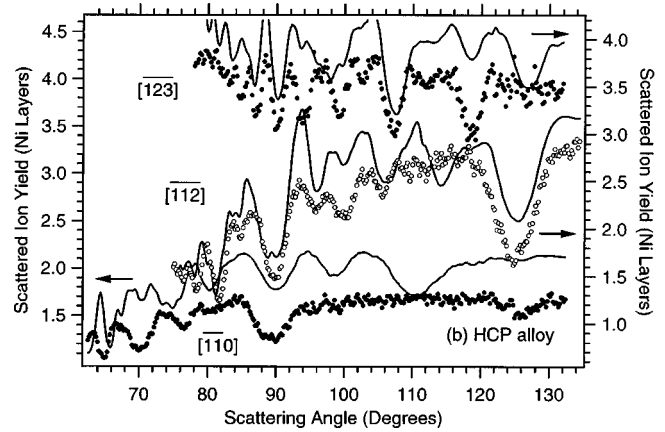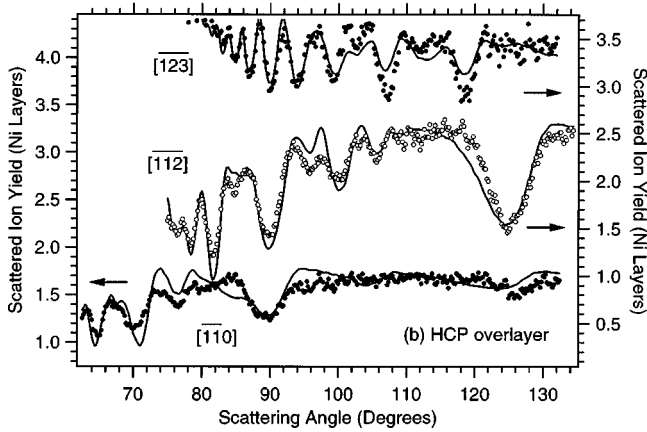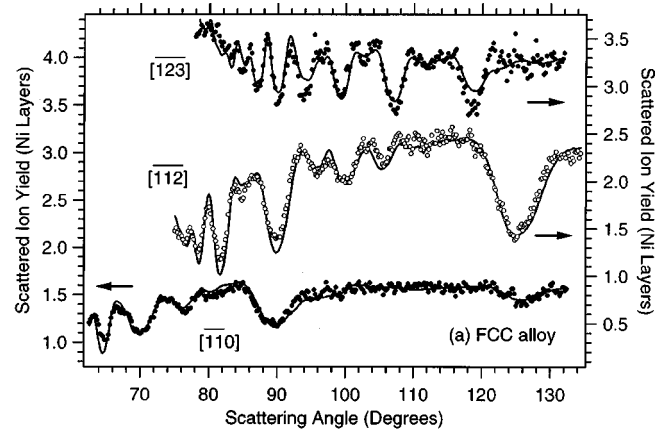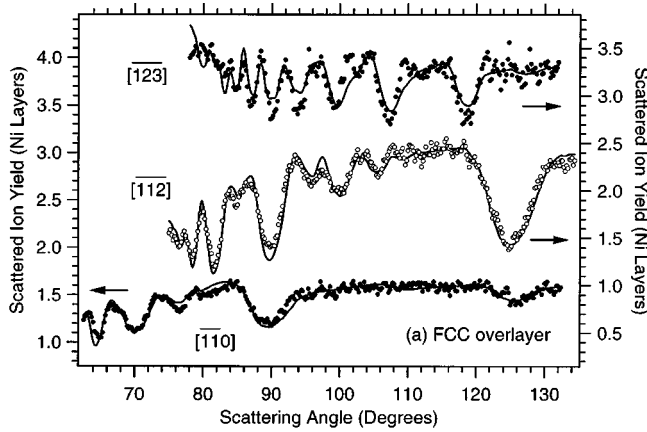
FIG. 3. Experimental blocking curves (data points) obtained from a Ni(111)($\sqrt{3}\times\sqrt{3}$)$R30°$-Pb surface using incident 100 keV H$^+$ ions, together with the corresponding best-fit simulations (solid curves) for (a) fcc overlayer and (b) hcp overlayer structural models. Incident ions were aligned along $[\bar{1}\bar{1}0]$ (left-hand ordinate) and $[\bar{1}\bar{1}\bar{2}]$, $[\bar{1}\bar{2}\bar{3}]$ (right-hand ordinate) crystallographic directions. Scattering angles for most of the bulk blocking directions are summarized in Figs. 1 and 2.

et al. have suggested that it results from a random replacement of Pb by Ni in the ($\sqrt{3}\times\sqrt{3}$)$R30°$ structure.[21]

Figure 3 shows a comparison of experimental blocking curves with best-fit simulations for the fcc and hcp overlayer structures in the $[\bar{1}\bar{1}0]$, $[\bar{1}\bar{1}\bar{2}]$, and $[\bar{1}\bar{2}\bar{3}]$ incidence geometries. Figure 4 shows the corresponding comparisons for the fcc and hcp surface alloy models. As remarked earlier, the calculation of R_χ is based on actual number of detected scattered ions, so the application of the calibration factor is used to adjust the theoretical yields (in layers) to these units. However, because of the strong angular dependence of the scattering cross section, the blocking curves in this form are superimposed on a steeply falling cross-section curve. Visual comparison of the blocking curve features is therefore greatly improved by displaying the scattered yields in terms of layers seen, leaving the theoretical curves as calculated, and applying the calibration factor [including the $\sin^4(\Phi_s/2)$ dependence on scattering angle] to the experimental yields. The comparisons shown are based on structural optimization to minimize the value of R_χ using the experimentally determined value of the calibration factor λ, allowing this factor to vary only by $\pm5\%$ about this absolute calibration.

FIG. 4. Experimental blocking curves from Ni(111)($\sqrt{3}\times\sqrt{3}$)$R30°$-Pb as in Fig. 3 compared with the best-fit simulations (solid curves) for (a) fcc alloy and (b) hcp alloy structural models.

The magnitude of this permitted adjustment of the scaling factor in our fitting procedure is clearly a significant parameter. If the allowed adjustment is smaller than the probable imprecision, the R factor may favor a structure that is fundamentally incorrect (but gives the best fit to the apparent absolute MEIS yields). If the allowed adjustment is too large, the fitting becomes determined only by the *structure* of the blocking curves, and fails to make use of the absolute yield calibration. In fact the allowed variation of $\pm5\%$ is essentially identical to that proposed by other workers in the MEIS technique,[23,28,30,31] and is consistent with the variation we see in our two alternative means of calibration, which must result from a combination of experimental factors including the perfection of the samples as well as aspects of the instrumentation. In the present case additional errors in this yield may stem from incomplete Pb coverage of the surface in the ordered phase.

Table I lists the best-fit structural parameters for each model, together with the associated global R_χ values, obtained by combining individual R_χ values from all three incidence geometries. Details of the method of combining R_χ values and the subsequent determination of experimental uncertainties are given elsewhere.[3,7] Structural parameters and R factors have been determined both with (bold text) and without (normal text) absolute calibration of the yield. It is immediately clear from both visual assessment of the fits and the associated R factors that the hcp overlayer and (hcp)

TABLE I. A summary of optimum structural fit parameters and associated R_χ values for each of the four models tested for the Ni(111)$(\sqrt{3}\times\sqrt{3})R30°$-Pb surface phase. Structural parameters and R factors listed in lightface text were obtained by using the experimental/theory scaling factor as a free parameter of the fitting (λ variable). Structural parameters and R factors listed in boldface text were obtained after application of a calibrated scaling factor to the theoretical curves during the fitting process (λ fixed) as described in the text.

Model	z_{Pb} (Å)	z_{12} (Å)	R_χ
fcc	2.55 ± 0.16[a]	1.97 ± 0.04	3.8
overlayer	$\mathbf{2.55\pm0.16}$[a]	$\mathbf{1.97\pm0.04}$	$\mathbf{3.8}$
hcp	3.12 ± 0.13[a]	1.97 ± 0.04	9.2
overlayer	$\mathbf{3.10\pm0.12}$[a]	$\mathbf{1.98\pm0.03}$	$\mathbf{9.6}$
fcc alloy	2.57 ± 0.16[b]	1.97 ± 0.05	3.9
	$\mathbf{2.64\pm0.14}$[b]	$\mathbf{1.99\pm0.05}$	$\mathbf{4.0}$
hcp alloy	2.50 ± 0.10[b]	1.96 ± 0.07	19.7
	$\mathbf{2.60\pm0.10}$[b]	$\mathbf{2.11\pm0.07}$	$\mathbf{79.3}$

[a]For overlayer models, z_{Pb} is the layer spacing of the Pb relative to the outermost Ni layer, and z_{12} is the first-to-second Ni layer spacing.

[b]For alloy models, z_{Pb} is the layer spacing of the Pb atoms relative to the outermost complete Ni layer and z_{12} is the layer spacing of the Ni atoms in the alloy layer relative to this same outermost complete Ni layer.

stacking-fault alloy phases can be rejected. The distinction between the fcc overlayer and fcc alloy results, however, is more marginal. The overlayer model actually yields the lowest global R factor; however, for the overlayer model the minimum R factor is 3.8 but the error analysis reveals that structures with R factor values less than 4.8 lie within the range of precision, and this clearly includes the value of 4.0 found for the alloy model. Indeed, with some relaxation of the absolute calibration scaling the R factor for the alloy model is even closer at 3.9. Formally, therefore, this analysis is unable to distinguish between these two structural models.

The problem of distinguishing between fcc overlayer adsorption and (fcc site) substitution in the surface using MEIS is one we have discussed in the past.[7] The essential problem is that in most scattering geometries one does not detect directly the relative positions of atoms in (approximately) the same plane parallel to the surface, so one does not distinguish between an outer layer comprising only 0.33 ML of adsorbate and one in which the outer layer also contains 0.67 ML of substrate atoms in essentially bulk-terminated sites. One might imagine that the substitution of one-third of the outermost Ni atoms by Pb would lead to a pronounced reduction in the predicted scattering yield from Ni atoms, but because the substitutional Pb atoms have a different layer spacing relative to the extended Ni bulk, they do not shadow subsurface atoms along the low-index incidence directions (apart from normal incidence), so the missing Ni scattering signal from the top layer is simply replaced by an equivalent signal from a lower layer. The effect of forming the surface alloy as opposed to forming an overlayer is thus to simply transpose perpendicular to the surface by one layer spacing some of the shadowing and blocking events that determine the scattering yield between the two models. Distinguishing
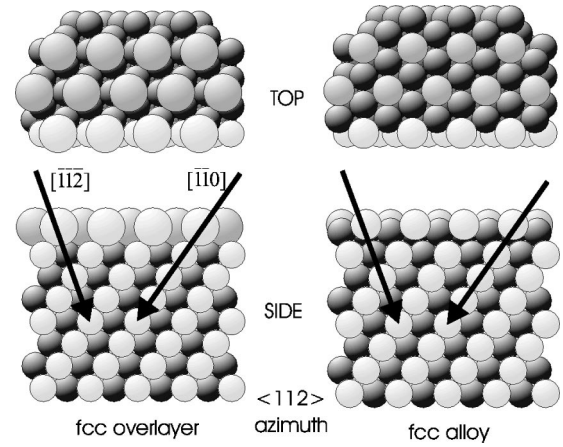

FIG. 5. Plan and sectional views of the fcc overlayer and fcc substitutional alloy models of the Ni(111)$(\sqrt{3}\times\sqrt{3})R30°$-Pb surface (Ni atoms smaller dark balls, Pb atoms larger lighter balls) showing the scattering plane of atoms including the Pb adsorbate atoms within the $\langle112\rangle$ azimuth. The atoms within this plane (both Pb and Ni if coplanar) are shown as very light for clarity. Note that in the alloy model the Pb adsorbates have been drawn with reduced-size spheres to avoid overlapping, a direct manifestation of the apparent size reduction in this model as discussed in the text.

between these two structures therefore requires a careful choice of scattering geometry. Indeed, in our initial measurements on this system we first measured only the $[\bar{1}\,\bar{1}0]$ and $[\bar{1}\,\bar{1}\,\bar{2}]$ incidence geometries, and noted the insensitivity of the results to this aspect of the structure, which is evident in the theoretical fits for these two structures in Figs. 3 and 4.

We therefore undertook a series of model calculations to check the sensitivity of other geometries to this difference in structure; these calculations showed that the $[\bar{1}\,\bar{2}\,\bar{3}]$ incidence geometry displays the required sensitivity. The key reason for this is that while the $[1\,\bar{1}0]$ and $[\bar{1}\,\bar{1}\,\bar{2}]$ incidence directions lie in a $\langle112\rangle$ azimuth, the $[\bar{1}\,\bar{2}\,\bar{3}]$ direction lies in a $\langle110\rangle$ azimuth. In the $\langle112\rangle$ azimuths for a clean surface all planes perpendicular to the surface that cut through the atoms are identical and contain atoms in all layers (see Fig. 1). If we form a $(\sqrt{3}\times\sqrt{3})R30°$ structure on the surface, this situation changes in that $\frac{2}{3}$ of such planes then contain only substrate atoms, whereas the other $\frac{1}{3}$ contain only adsorbate atoms in the top layer. This is true for both fcc hollow sites and substitutional sites, so there is no fundamental difference in these two structures; the relevant planes of atoms containing the Pb adsorbates for these two models are shown in Fig. 5. In the case of the $\langle110\rangle$ azimuth, on the other hand, there are three distinct planes of this type even for the clean surface (see Fig. 2), because only every third layer falls in a single plane; these three planes thus contain atoms in layers 1,4,7, etc., 2,5,8, etc. and 3,6,9, etc. Forming the $(\sqrt{3}\times\sqrt{3})R30°$ surface structure also modifies only one of these planes. However, the modification is different for substitutional or fcc hollow-site occupation (Fig. 6). In the substitutional case, layer 1 of the clean surface is modified so the first of these planes is changed; in the case of a fcc overlayer an extra adsorbate layer is added to the plane containing substrate layers 3,6,9 etc. Moreover, in the substitutional alloy case the $\langle110\rangle$ section containing layer 1 contains both
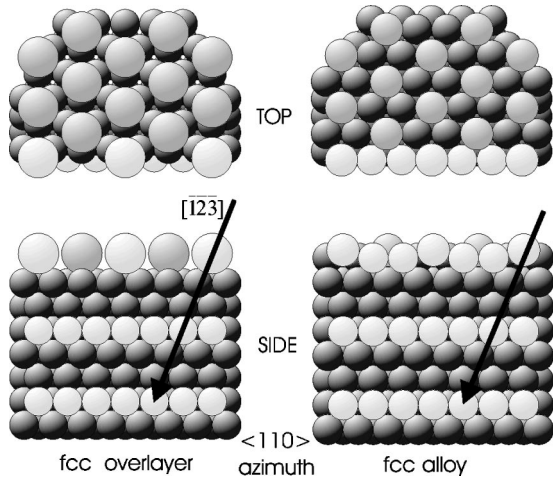
FIG. 6. Plan and sectional views of the fcc overlayer and fcc substitutional alloy models of the Ni(111)($\sqrt{3}\times\sqrt{3}$)R30°-Pb surface as in Fig. 5, but for scattering in the $\langle 110\rangle$ azimuthal plane.

adsorbate and substrate atoms in the top layer, so blocking events involving both adsorbate and substrate atom scatterers in the top plane are involved. Scattering in the $\langle 110\rangle$ azimuths thus has a far greater potential to distinguish between the fcc overlayer and alloy models.

Comparison of the simulated $[\bar{1}\,\bar{2}\,\bar{3}]$ blocking curve for the fcc overlayer and alloy models, as shown in Figs. 3 and 4, illustrates this rather clearly. Particularly in the scattering angle range from about 95° to 120° there are very marked differences, the overlayer showing single peaks with shoulders, while the alloy phase shows double peaks. The quantitative fits in this scattering geometry are less good than in the others, but the scattering yields in the $[\bar{1}\,\bar{2}\,\bar{3}]$ incidence direction are much larger than in the other directions used, so the blocking dips are proportionally smaller; this accounts for the fact that the associated R factors are quite low despite the visual impression of poorer fits. Despite this, it is clear that the experimental data are much more similar to those for the surface alloy phase in this region. This qualitative preference is also reflected in the values for the R factor evaluated for this scattering geometry alone (see Table II), the value being 3.1 for the fcc overlayer model but only 2.3 for the alloy. We therefore conclude that while the global R factor for the full data analysis does not formally distinguish these models, the one data set that shows significant sensitivity to this aspect clearly favors the fcc surface alloy phase.

TABLE II. Values of R factors for the individual blocking curves corresponding to the structural models defined in Table I (λ fixed).

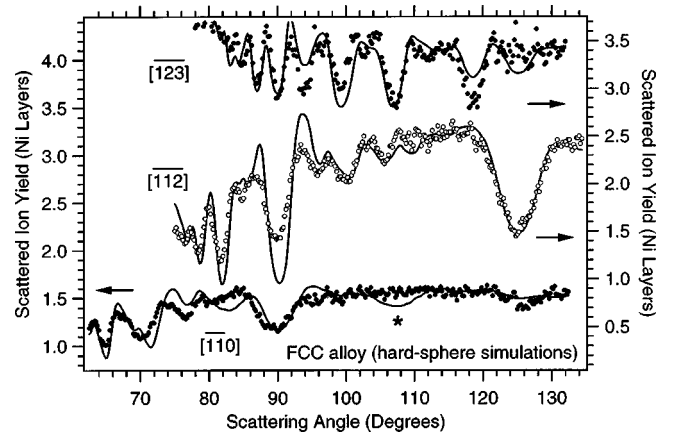| Model	$R_{[\bar{1}\,\bar{1}0]}$	$R_{[\bar{1}\,\bar{1}\,\bar{2}]}$	$R_{[\bar{1}\,\bar{2}\,\bar{3}]}$	R_{total}
fcc overlayer	4.2	4.1	3.1	3.8
hcp overlayer	15.0	9.2	3.1	9.6
fcc alloy	4.3	5.3	2.3	4.0
hcp alloy	147.6	41.4	32.9	79.3

FIG. 7. Comparison of the experimental blocking curves with the results of a simulation based on a fcc alloy model with the very large corrugation amplitude expected for Ni and Pb atoms in the surface layer having their bulk metallic radii. Notice, in particular, the predicted Pb blocking dip for $[\bar{1}\,\bar{1}0]$ incidence at a scattering angle of around 107° (marked with an asterisk) which is not seen in the experimental data.

IV. GENERAL DISCUSSION

While our conclusion that a substitutional surface alloy structure is favored is in qualitative agreement with that of the earlier low-energy ion scattering experiment,[21] the actual structural parameter values we find differ significantly from those of the earlier study. In particular, we find the alloy layer corrugation to be 0.65 ± 0.15 Å, very significantly larger than the value of 0.2 Å derived from ICISS [although it is similar to reported corrugations[6,7] of 0.60 or 0.47 Å for the (stacking-faulted) surface alloy Cu(111)($\sqrt{3}\times\sqrt{3}$)R30°-Sb]. The origin of such a large discrepancy is unclear; MEIS certainly can be expected to be capable of yielding greater precision than ICISS due to better knowledge of the interaction potential at high energies, but the precision in ICISS is expected to be higher than the magnitude of this difference.

The actual magnitude of this corrugation, however, is rather surprisingly small if we compare it with the value of 1.67 Å that is to be expected for a hard-sphere model based on the metallic radii of the Ni and Pb atoms discussed earlier. Indeed, our structural solution, assuming that the effective radius of the outermost Ni atoms is unchanged from that of the bulk, implies an effective radius of the incorporated Pb atoms of 1.33 ± 0.04 Å, to be compared with the value in bulk Pb of 1.75 Å. The alloy layer corrugation of 0.2 Å found in the ICISS study by Umezawa *et al.*[21] would actually imply an even smaller effective radius of only 1.25 Å, but these authors do not comment on the result. By contrast, we note that the best-fit fcc overlayer model implies a much more reasonable effective radius for the adsorbed Pb of 1.67 ± 0.14 Å, a comparison which seems to favor this solution on physical grounds. We should stress, however, that our data clearly exclude the possibility that a surface alloy forms with the very large corrugation amplitude expected from application of the bulk metallic radii. A specific illustration of this is shown in Fig. 7 in which the consequences of such a model are compared with the experimental blocking curves. For the $[\bar{1}\,\bar{1}0]$ incidence direction, the dominant

TABLE III. Interatomic (*A-B*) distances in surface alloys formed by the deposition of element *B* on the surface of element *A* for several previously studied systems, and for the present work marked with an asterisk.

Substrate (*A*)	Adsorbate (*B*)	Surface phase	d_{A-B} (Å) surface	d_{A-B} (Å) at. radii	d_{A-B} (Å) cov. radii
Cu(100)	Au	$c(2\times2)$	2.55[a]	2.73	2.51
Cu(100)	Mn	$c(2\times2)$	2.58[a]	2.62	2.34
Cu(111)	Sb	$(\sqrt{3}\times\sqrt{3})R30°$	2.60[b]	2.86	2.57
Ag(111)	Sb	$(\sqrt{3}\times\sqrt{3})R30°$	2.89[c]	3.03	2.74
Ni(111)	Pb	$(\sqrt{3}\times\sqrt{3})R30°$	2.57*	3.00	2.62

[a]Reference 3.
[b]References 6,7.
[c]Reference 6.

blocking feature of the simulation is the strong dip at a scattering angle of 90° corresponding to the bulk [001] emergence direction, but the large displacement of the Pb atoms perpendicular to the surface leads to an additional blocking dip displaced to a scattering angle of 107°, which is clearly not present in the experimental data. Evidently, minor adjustments of this structure will not rectify this major discrepancy.

Although the phenomenon of surface alloying has been recognized as widespread, the number of cases in which complete structural information is available is more limited. One group of systems that have been considered in some detail is the alkali metals on Al(111), but the alkalis are a rather special case in that they have very low electronegativity and a strong propensity to form ions, even when adsorbed on metal surfaces. Moreover, because of their single outershell *s* electron, there is a very large difference (typically approximately 1.0 Å) between the ionic and metallic radii. The consistent pattern for the surface alloys formed by Na, K, and Rb on Al(111) is that the effective radii for the alkali adsorbates are slightly smaller than, but close to, the metallic values. However, systems of essentially ionic character are not really relevant to the present system (Ni and Pb having identical electronegativity values).

Table III summarizes the results of other substitutional surface alloy systems for which there are quantitative data. The actual substrate-adsorbate (*A-B*) nearest-neighbor distances found in these studies are compared in this table with the values to be expected on the basis of the sums of the atomic radii and the sums of the covalent radii, the atomic radii being given (as is common for tabulations on periodic table charts[32]) as the metallic radii for a coordination number of 12 (with corrections according to Pauling's formula[33] for materials that do not form fcc or hcp solids with this coordination). What is clear from these comparisons is that the general trend is for the surface alloy phase to show a significant shortening of the bond length relative to that predicted by the sum of the atomic (metallic) radii. The one exception is the case of the Cu(100)$c(2\times2)$-Mn surface phase in which the Cu-Mn bond length is actually almost identical to this predicted value; in this special case theoretical modeling shows that the Mn effective radius *is* significantly larger than would normally be expected due to a modified magnetic state of the Mn atom in this phase.[16]

In part, the shorter interatomic distances seen in Table III must reflect the fact that for dissimilar materials the bonding in the alloy must be, at least to some degree, covalent, and the sum of the covalent radii is significantly shorter, as is also shown in the table. This is especially true for the cases of Cu-Sb, Ag-Sb, and Ni-Pb; standard texts on crystalline structures distinguish between alloys involving two true metals (which include all the noble and transition metals) and those involving a true metal and a so-called *B* subgroup element from further to the right of the periodic table, including elements in groups IVA and VA such as Pb and Sb.[34] Indeed, in the case of Cu-Sb this is reflected also in bulk intermetallic phases; the Cu-Sb bond length in bulk Cu$_2$Sb is 2.62 Å,[35] very close to the actual value found in the surface phase and also to the sum of the covalent radii, and much less than the sum of the atomic radii. By contrast, however, it is notable that in the Cu-Au system, which is a case of an alloy of two true metals, the Cu-Au bond length in the ordered Cu$_3$Au alloy is 2.82 Å, which is actually larger than the sum of the atomic radii and thus substantially larger than in the case of the Cu(100)$c(2\times2)$-Au surface alloy phase. Indeed, this surface phase is notable in that there is essentially no corrugation of the surface alloy layer despite the large difference in atomic radii (1.28 and 1.46 Å) of the constituents. Clearly, therefore, there is some additional factor at the surface which tends to lower the corrugation and the associated interatomic bond length relative to the bulk alloy phase (in cases where such an alloy phase exists).

Recent understanding of surface stress in metallic surfaces suggests a simple reason for this effect. It seems now to be rather well established that clean unreconstructed elemental metal surfaces are in a state of tensile stress.[36] This is attributed to the fact that the valence charge density at the surface is lower than in the bulk due to the spillover into the vacuum, but the equilibrium spacing of the atoms in the bulk is related to the optimum value of the surrounding valence charge density. Some contraction of the outermost layer spacing can help to relieve this problem, but the atoms would still prefer to have a shorter spacing parallel to the surface. In some cases [such as Au(111) and Au(100) surfaces] this effect can lead to a reconstruction of the surface layer to a (more) close-packed overlayer. However, in most systems the surface atoms that are under tensile stress are locked in the periodic potential of the underlying bulk. If we now substitute some fraction of the atoms in such a surface by those of another metallic element with a larger radius, it is clear

that the need to immerse these atoms in a high valence charge density will tend to draw them into the surface layer. While this should, in part, be countered by a tendency to introduce lateral repulsion and thus compressive surface stress, the intrinsic tensile stress of the clean surface will also moderate this effect. In this context it is worth noting that for a surface alloy layer with a small corrugation, the inter-atomic bond length changes very little for a much larger change in the corrugation amplitude. Thus, while in the $Cu(100)c(2\times2)$-Au phase the corrugation amplitude is less than 0.1 Å, in $Cu(100)c(2\times2)$-Mn this corrugation is 0.3 Å but the interatomic bond length is only 0.03 Å larger (see Table III). From the point of view of maximizing the valence charge density around the substitutional atom, the corruga-tion amplitude is probably even more important than the in-teratomic spacing, an observation that highlights the previ-ously recognized anomalous behavior of this Cu/Mn surface phase.

Returning to the specific case of the Ni/Pb surface alloy studied here, we conclude that the apparent large reduction in the Pb effective radius relative to its bulk metallic value can be reconciled, at least qualitatively, in terms of two ef-fects. One of these is that this phase does not involve two true metals and may be expected to show a significant degree of covalent character in the bonding. The other is the surface effect of maximizing the valence charge density around the surface atoms, which favors a more nearly coplanar surface alloy phase. Some limited specific evidence for the former contribution comes from a study of the bulk crystallography of a NiPb phase. Although the equilibrium phase diagram of the Ni-Pb system shows very limited ($<3\%$) solid solubility of Pb in Ni,[37] this NiPb phase, which is presumably meta-stable, was produced by vacuum evaporation, and was found to have the NiAs structure with $a = 4.15$ Å, $c = 5.28$ Å,[38] leading to an implied Ni-Pb nearest-neighbor distance of 2.73 Å, significantly closer to the sum of the covalent radii than the sum of the atomic radii (Table III).

Superficially, at least, a quantitative LEED study of the $Cu(100)c(4\times4)$-Pb phase[39] appears to offer quite conflict-ing evidence. In this system the authors also concluded that a surface alloy phase is formed, but the Cu-Pb nearest-neighbor distances found were around 2.9 Å, much closer to the sum of the atomic radii (3.02 Å) than in our Ni-Pb case. This surface phase is rather different, however, in two ways. First, it contains close-packed rows of Pb atoms, so the ad-sorbate atoms are not coordinated only to substrate atoms as in all the other systems we have considered. In addition, however, the surface layer is not formed simply by substitut-ing substrate Cu atoms by Pb, but actually comprises a mixed Cu-Pb layer with a different atomic density from the underlying Cu(100). Of course, there are also important dif-ferences in the bonding character and chemistry of Ni and Cu, but in general terms this surface alloy phase is quite different from the substitutional structures which have formed the basis of our discussion.

V. CONCLUSION

Our MEIS structural investigation of the $Ni(111)(\sqrt{3} \times\sqrt{3})R30°$-Pb surface phase was motivated by a desire to answer two questions: does this phase involve the formation of a substitutional surface alloy, as deduced in an earlier coaxial impact collision ion scattering spectroscopy (CA-ICISS) study by Umezawa et al.,[21] and if so does this surface alloy also have an associated stacking fault relative to the underlying substrate, as has been found for similar phases formed by Sb on Cu(111) and Ag(111)? The answer to the latter question is clear; we can safely reject models based on hcp site occupation of the Pb adsorbate, either as an over-layer or as a substitutional alloy. The clear distinction be-tween the fcc overlayer and fcc substitutional alloy models proves more difficult. Formally, the MEIS data analysis based on the global R factor does not allow the distinction to be made, and actually marginally favors the simple over-layer. On the other hand, a subset of data taken in a scatter-ing geometry chosen to be especially sensitive to this key question does clearly favor the alloy phase interpretation.

At first glance, a very surprising consequence of this con-clusion is that the associated quantitative structural param-eters indicate that the Pb atoms in this phase have effective radii which are some 0.4 Å smaller than in bulk crystalline Pb. However, comparison with the limited results of other quantitative structural studies of substitutional surface alloys leads to the conclusion that this result may not be anomalous, but may be a consequence of a combination of partial cova-lent bonding and a general trend to reduce surface corruga-tion amplitudes in such systems to optimize the bonding and associated total energy.

Despite this rationalization, it is clear that the $Ni(111) \times(\sqrt{3}\times\sqrt{3})R30°$-Pb surface phase is a case where a distinc-tion between adsorbed overlayer and substitutional alloy structure is crucial as it provides a completely different view of the surface bonding. By choosing an appropriate scatter-ing geometry we have tried to overcome a potential weak-ness of the MEIS technique in order to distinguish these structures, and clearly do favor the alloy phase interpretation. An earlier CAICISS study led to the same conclusion, but with substantial and puzzling differences in the quantitative structural parameter values. Evidently, it would be interest-ing to test this conclusion with a technique based on funda-mentally different physical principles. In view of the large difference in atomic number of Ni and Pb and the fact that the phase does show good long-range order, quantitative LEED may be well suited to applying this additional test.

ACKNOWLEDGMENTS

[1] Z. Q. Wang, Y. S. Li, C. K. C. Lok, J. Quinn, and F. Jona, Solid State Commun. **62**, 181 (1987).

[2] J. G. Tobin, J. C. Hansen, and M. K. Wagner, J. Vac. Sci. Technol. A **8**, 2494 (1990).

[3] D. Brown, T. C. Q. Noakes, D. P. Woodruff, P. Bailey, and Y. Le Goaziou, J. Phys.: Condens. Matter **11**, 1889 (1999).

[4] M. Wuttig, C. C. Knight, T. Flores, and Y. Gauthier, Surf. Sci. **292**, 189 (1993).

[5] R. Toomes, A. Theobald, R. Lindsay, T. Giessel, O. Schaff, R. Didszhun, D. P. Woodruff, A. M. Bradshaw, and V. Fritzsche, J. Phys.: Condens. Matter **8**, 10 231 (1996).

[6] S. A. DeVries, W. J. Huisman, P. Goedtkindt, M. J. Zwanenburg, S. L. Bennett, I. K. Robinson, and E. Vlieg, Surf. Sci. **414**, 159 (1998).

[7] P. Bailey, T. C. Q. Noakes, and D. P. Woodruff, Surf. Sci. **426**, 358 (1999).

[8] T. C. Q. Noakes, D. A. Hutt, C. F. McConville, and D. P. Woodruff, Surf. Sci. **372**, 117 (1997).

[9] E. Soares *et al.* (unpublished).

[10] A. Schmalz, S. Aminpirooz, L. Becker, J. Haase, J. Neugebauer, M. Scheffler, D. R. Batchelor, D. L. Adams, and E. Bogh, Phys. Rev. Lett. **67**, 2163 (1991).

[11] M. Kerkar, D. Fisher, D. P. Woodruff, R. G. Jones, R. D. Diehl, and B. Cowie, Phys. Rev. Lett. **68**, 3204 (1992).

[12] J. Burchhardt, M. M. Nielsen, D. L. Adams, E. Lundgren, and J. N. Andersen, Phys. Rev. B **50**, 4718 (1994).

[13] C. Stampfl, M. Scheffler, H. Over, J. Burchhardt, M. M. Nielsen, D. L. Adams, and W. Moritz, Phys. Rev. Lett. **69**, 1532 (1992).

[14] M. M. Nielsen, J. Burchhardt, D. L. Adams, E. Lundgren, and J. N. Andersen, Phys. Rev. Lett. **72**, 3370 (1994).

[15] G. Scragg, B. C. C. Cowie, M. Kerkar, D. P. Woodruff, A. Daimellah, S. Turton, and R. G. Jones, J. Phys.: Condens. Matter **6**, 1869 (1994).

[16] M. Wuttig, Y. Gauthier, and S. Blügel, Phys. Rev. Lett. **70**, 3619 (1993).

[17] H. A. van der Vegt, H. M. van Pinxteren, M. Lohmeier, E. Vlieg, and J. M. C. Thornton, Phys. Rev. Lett. **68**, 3335 (1992).

[18] J. Vrijmoeth, H. A. van der Vegt, J. A. Meyer, E. Vlieg, and R. J. Behm, Phys. Rev. Lett. **72**, 3843 (1994).

[19] S. Oppo, V. Fiorentini, and M. Scheffler, Phys. Rev. Lett. **71**, 2437 (1993).

[20] A very recent SXRD study concludes that $Ag(111)(\sqrt{3} \times \sqrt{3})R30°$-Sb is a simple surface alloy phase, but does not discuss the possible stacking-fault model: I. Meunier, J.-M. Gay, L. Lapena, B. Aufrey, H. Oughaddou, E. Landemark, G. Falkenberg, L. Lottermoser, and R. L. Johnson, Surf. Sci. **422**, 42 (1999).

[21] K. Umezawa, S. Nakanishi, T. Yumura, W. M. Gibson, M. Watanabe, Y. Kido, S. Yamamoto, Y. Aoki, and H. Naramoto, Phys. Rev. B **56**, 10 585 (1997).

[22] K. Umezawa, A. Takahashi, T. Yumura, S. Nakanishi, and W. M. Gibson, Surf. Sci. **365**, 118 (1996).

[23] J. F. Van der Veen, Surf. Sci. Rep. **5**, 199 (1985).

[24] P. R. Watson, J. Phys. Chem. Ref. Data **19**, 85 (1990).

[25] R. M. Tromp and J. F. Van der Veen, Surf. Sci. **133**, 159 (1983).

[26] D. P. Jackson, Surf. Sci. **43**, 431 (1974).

[27] T. C. Q. Noakes, P. Bailey, and D. P. Woodruff, Nucl. Instrum. Methods Phys. Res. B **136–138**, 1125 (1998).

[28] M. Chester and T. Gustaffson, Surf. Sci. **256**, 135 (1991).

[29] T. Narusawa, W. M. Gibson, and E. Tornqvist, Surf. Sci. **114**, 331 (1982).

[30] J. W. M. Frenken, R. G. Smeenk, and J. F. Van der Veen, Surf. Sci. **135**, 147 (1983).

[31] J. V. Barth and D. E. Fowler, Phys. Rev. B **52**, 1528 (1995).

[32] For example, periodic table chart from Sargent-Welch Scientific Co., catalogue number S-18806.

[33] L. Pauling, *The Nature of the Chemical Bond*, 3rd ed. (Cornell University Press, Ithaca, NY, 1960).

[34] R. C. Evans, *An Introduction to Crystal Chemistry*, 2nd ed. (Cambridge University Press, Cambridge, 1966), Chap. 13.

[35] R. W. G. Wyckoff, *Crystal Structures*, 2nd ed. (Wiley Interscience, New York, 1965), Vol. 1.

[36] H. Ibach, Surf. Sci. Rep. **29**, 193 (1997).

[37] *Binary Alloy Phase Diagrams*, edited by T. B. Masralski (American Society for Metals, Metals Park, OH, 1986).

[38] R. R. Bitti, J. Dixmier, and A. Guiner, C. R. Acad. Sci., Ser. II: Mec., Phys., Chim., Sci. Terre Univers **266**, 565 (1986).

[39] Y. Gauthier, W. Moritz, and W. Hösler, Surf. Sci. **345**, 53 (1996).